

# Energy scaling in a compact bulk multi-pass cell enabled by Laguerre-Gaussian single-vortex beams

V. Koltalo,<sup>1</sup> S. Westerberg,<sup>2</sup> M. Redon,<sup>2</sup> G. Beaufort,<sup>2</sup> A.-K. Raab,<sup>2</sup> C. Guo,<sup>2</sup> C. L. Arnold,<sup>2</sup> and A.-L. Viotti<sup>\*2</sup>

<sup>1</sup>Laboratoire d'Optique Appliquée (LOA), Institut Polytechnique de Paris, ENSTA Paris - CNRS - Ecole Polytechnique, 91120 Palaiseau, France

<sup>2</sup>Department of Physics, Lund University, P.O. Box 118, SE-22100 Lund, Sweden

(\*victor.koltalo@ensta-paris.fr, anne-lise.viotti@fysik.lth.se)

(Dated: 18 December 2024)

We report pulse energy scaling enabled by the use of Laguerre-Gaussian single-vortex ( $LG_{0,l}$ ) beams for spectral broadening in a sub-40 cm long Herriott-type bulk multi-pass cell. Beams with orders  $l = 1 - 3$  are generated by a spatial light modulator, which facilitates rapid and precise reconfiguration of the experimental conditions. 180fs pulses with 610 $\mu$ J pulse energy are post-compressed to 44fs using an  $LG_{0,3}$  beam, boosting the peak power of an Ytterbium laser system from 2.5GW to 9.1GW. The spatial homogeneity of the output  $LG_{0,l}$  beams is quantified and the topological charge is spectrally-resolved and shown to be conserved after compression by employing a custom spatio-temporal coupling measurement setup.

## I. INTRODUCTION

Ytterbium (Yb)-doped amplified laser systems have proven to be on the cutting edge for efficient high repetition rate - high power laser technology, enabling high-order harmonics generation (HHG) at high flux<sup>1</sup> and kHz laser-plasma acceleration (LPA)<sup>2</sup>. However, the narrow spectral bandwidth of these systems leads to pulse durations of several hundreds of femtoseconds (fs), constraining the usable peak powers of such sources.

In order to overcome this limitation, pulse post-compression methods can be used<sup>3</sup>. The multi-pass cell (MPC) technique<sup>4,5</sup>, based on self-phase modulation (SPM), exhibits high compression ratios, excellent spatio-spectral qualities and high throughput. Most MPCs employ a Herriott geometry<sup>6</sup>, and consist of two concave mirrors forming a stable resonator that maintains an eigenmode and contains a Kerr medium. The SPM is incremented multiple times along the folded optical path inside the cell, with a non-linear medium that can either be a gas or a bulk material. Gas MPCs are the most recurrent type of cell, allowing the combination of GW-input peak powers and high pulse energies<sup>7,8</sup> to reach large output peak powers up to the sub-TW regime<sup>9</sup> and few cycle pulse durations<sup>10</sup>. With this comes the cost of an extended footprint and the use of rare gases, usually neon or argon, requiring vacuum or high-pressure equipment. Bulk MPCs, on the other hand, are less common for large peak power increases due to their apparent lack of energy scalability. They originally operate with MW-input peak powers<sup>11</sup> since a bulk material, as opposed to gas, cannot sustain high power or forgive an excess of intensity without getting permanently damaged. A widely-used non-linear medium in bulk MPCs is Fused Silica (FS), which exhibits a critical power for self-focusing of  $P_{\text{crit}} = 4.16\text{MW}$  at 1030nm<sup>12</sup>. To reach high peak power outputs in bulk MPCs, the system has to be operated with input powers much greater than  $P_{\text{crit}}$ <sup>13</sup>, which becomes challenging for managing self-focusing and mirror damages. To mitigate these issues, one can reduce the effect of self-focusing by enlarging the beam size, thereby extending

the length of the MPC, or by changing the position and thickness of the bulk medium to allow smaller increments of non-linearity<sup>13</sup>. To comply with the inherent lensing from the Kerr medium, one also needs to use non-linear mode-matching<sup>14,15</sup> to adapt the beam input parameters to the complete system.

As a result, the scalability in energy of bulk MPCs is still to be addressed in order to compete with the parameter range of gas MPCs and other post-compression systems, such as gas-filled hollow-core fibers (HCF)<sup>16</sup>. So far, the maximum reported input pulse energy is 400 $\mu$ J in a hybrid air-bulk Herriott configuration<sup>17</sup>. To further increase the input energy, multiple approaches can be envisioned, such as convex-concave geometries<sup>18,19</sup>, hybrid MPCs<sup>15,17</sup>, bow-tie geometries<sup>20,21</sup>, temporal pulse division<sup>22</sup> and spatial shaping<sup>23</sup>. The latter technique was demonstrated in a gas MPC by employing a Laguerre-Gaussian  $LG_{0,1}$  mode generated by a spiral phase plate to spread the energy on the transverse plane, showing the compressibility of 112mJ, 1.3ps pulses down to 37fs<sup>23</sup>.

In this work, we extend the approach of spatial shaping to bulk MPCs, using the versatility of a spatial light modulator (SLM) to study high-order Laguerre-Gaussian single-vortex beams ( $LG_{0,l}$ ,  $l = 1 - 3$ ). We report the post-compression of 180fs pulses with 610 $\mu$ J pulse energy, corresponding to 2.5GW input peak power, down to 44fs with high throughput, in a compact bulk MPC with a footprint smaller than 40cm, using a  $LG_{0,3}$  mode. This translates to an output peak power of 9.1GW with maintained spatial properties. We first describe the non-linear mode-matching conditions and the theoretical energy scaling allowed by  $LG_{0,l}$  beams. Then, we show the experimental realization and characterize the temporal and spatial profiles, showing similar results for all three orders. We also use a custom two-parameter characterization to quantify the spatial homogeneity after the MPC. Finally, we adapt a spatio-temporal couplings (STCs) measurement setup to  $LG_{0,l}$  beams and show that the transverse profile of a  $LG_{0,1}$  mode remains unchanged for different wavelengths. The beam's phase is also spectrally-resolved, demonstrating conservation of the topological charge through post-compression.

## II. THEORETICAL FRAMEWORK FOR ENERGY SCALING WITH $LG_{0,l}$ BEAMS

All simulations are based on the geometrical characteristics of the experimental setup, further discussed in III A.

### A. Description of Laguerre-Gaussian beams

The mathematical form of Laguerre-Gaussian beams is as follows:

$$LG_{m,l}(\rho, \phi, z) = G(\rho, \phi, z) \times \left(\frac{\rho}{W(z)}\right)^{|l|} L_m^{|l|}\left(\frac{2\rho^2}{W^2(z)}\right) \times \exp[-jl\phi + j(|l| + 2m)\zeta(z)] \quad (1)$$

where  $G(\rho, \phi, z)$  represents the amplitude of a Gaussian beam in the cylindrical coordinate system,  $L_m^{|l|}$  is the Laguerre polynomial, with  $m, l$  the radial and azimuthal orders of the considered Laguerre-Gaussian beam, and  $\zeta(z)$  is the Gouy phase. As we focus on the use of  $m = 0$  radial orders,  $LG_{0,l}$  beams are referred to as vortex of order  $l$  in the rest of the study. Both the critical power  $P_{\text{crit}}^{(l)}$  for self-focusing<sup>24</sup> and the beam size  $W^{(l)}(z)$ <sup>25</sup> depend on the vortex order, as:

$$P_{\text{crit}}^{(l)} = \frac{2^{2|l|+1}\Gamma(|l|+1)\Gamma(|l|+2)}{2\Gamma(2|l|+1)} P_{\text{crit}}^{(G)} \quad (2)$$

$$W^{(l)}(z) = \sqrt{|l|+1}W(z) = W_0\sqrt{|l|+1}\sqrt{1 + \left(\frac{z}{z_r}\right)^2} \quad (3)$$

where  $\Gamma$  is the Gamma function,  $W(z)$  the Gaussian beam size,  $W_0$  the waist size and  $P_{\text{crit}}^{(G)}$  the critical power for self-focusing of a Gaussian beam. For the same energy contained in the beam, the peak intensity of a vortex beam  $I^{(l)}$  will be lower than the Gaussian-equivalent peak intensity  $I^{(G)}$ , following the law:

$$\frac{I^{(l)}}{I^{(G)}} = \frac{|l|!}{(|l|/e)^{|l|}} \quad (4)$$

The theoretical intensity and phase maps of a vortex of order 1 are presented in Fig. 1 a) and b), and a visualization of Eq. 4 is provided in Fig. 1 c). It shows that, for the same pulse energy, the intensity is strongly reduced by using vortex beams compared to a Gaussian profile, and that higher-order vortices incrementally spread over larger spatial dimensions.

### B. Non-linear mode-matching with vortices

To efficiently propagate a laser beam in an MPC, mode-matching is required. In the case of bulk MPCs, lensing due to self-focusing in the bulk medium also needs to be taken

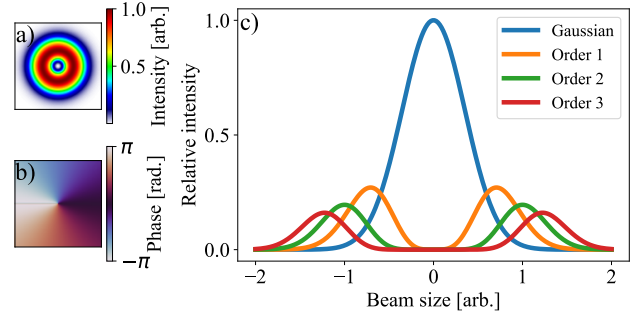


FIG. 1. a) Theoretical intensity and b) phase of a vortex of order 1. c) Relative intensities for a Gaussian mode and vortices of order  $l = 1 - 3$ , with the same pulse energy.

into account. This is referred to as non-linear mode-matching (NLMM)<sup>14,15</sup>. Compared to the Gaussian case, self-focusing is not as easily described, due to the orbital angular momentum (OAM) and the equivalent ring lens<sup>24</sup>. Yet, this particular self-focusing is still caused by the optical Kerr effect  $n = n_0 + n_2 I$  (where  $n$  is the refractive index of the material,  $n_0$  and  $n_2$  are the linear and non-linear refractive indices, and  $I$  is the intensity of the laser pulse), which is at the core of NLMM. A spatial propagation simulation with ideal vortex beams is performed for the MPC, disregarding temporal effects such as SPM or Group Delay Dispersion (GDD), to find the NLMM of the MPC. Self-focusing is simulated using the non-linear Schrödinger equation, solved using a 4th-order Runge-Kutta (RK4) scheme<sup>26</sup>. The MPC parameters mimic the experimental configuration, with a total of 14 passes through two 1 mm-thick plates of fused silica. A Bayesian Optimization algorithm<sup>27</sup> is employed to find the beam parameters (focus size and position) that reduce beam size variations on the mirrors from pass to pass. The use of such algorithm is of interest to converge towards the optimal parameters in a small number of steps, even in a multi-dimensional parameter space. If the cavity is linearly mode-matched, the self-focusing induced by a bulk material will shift the focus negatively, before the linear focus. Thus, the range of optimization given to the algorithm for the focus offset should be in the positive region. The waist size is also expected to vary, but its range is not restricted for the optimization.

In Fig. 2, the NLMM results are shown for the first three vortex orders, with pulse energies spanning from 150  $\mu\text{J}$  to 500  $\mu\text{J}$ . For each order and pulse energy, the waist size and focus offset that minimize the oscillations of the beam size on the mirrors over 14 passes are plotted in Fig. 2 a). We note that all vortex orders follow the same trend. Figure 2 b) and Fig. 2 c) display instead the optimization results as a function of the ratio of peak power to critical power  $P^{(l)}/P_{\text{crit}}^{(l)}$  for self-focusing in FS. In this case, clear linear correlations are observed. From this, we conclude that the NLMM in MPCs is not dependent on the vortex order but only on the ratio  $P^{(l)}/P_{\text{crit}}^{(l)}$ , which gives a recipe for a general mode-matching: by computing  $P^{(l)}/P_{\text{crit}}^{(l)}$  for a given vortex order, one can mode-match it to the MPC eigenmode by experimentally real-

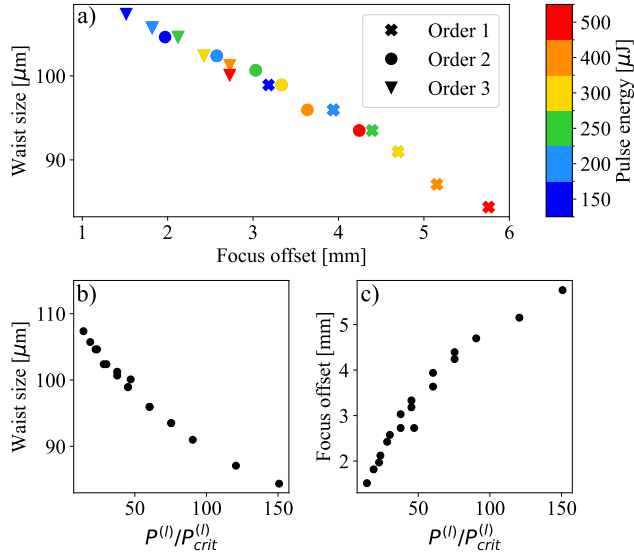


FIG. 2. a) Optimized waist size and focus offset of the beam. 0 mm corresponds to the linear mode-matching focus position. The pulse energies are ranging from 150  $\mu\text{J}$  to 500  $\mu\text{J}$ . Variation of b) the waist size and c) the offset in focus position in the cell as a function of the ratio of peak power  $P^{(l)}$  to critical power  $P_{\text{crit}}^{(l)}$  for self-focusing in FS, for the same range of pulse energies.

izing the corresponding beam size and focus position obtained from the optimization. This model can then be used to maximize the throughput of the experimental MPC and have a stable mode in the resonator. It is important to notice that these results are valid for one given geometry and dimensions of the system (cell length, position and thickness of the plates), and the same optimization has to be performed for each setup, which would end up in different values yet similar dynamics with respect to  $P^{(l)}/P_{\text{crit}}^{(l)}$ .

### C. Energy scaling in MPCs with vortices

The energy scaling factor is defined as the ratio between the vortex spectra energy and the Gaussian pulse energy for which the spectra of the two pulses have the same Fourier Transform Limit (FTL). To derive the energy scaling factor of each order, the RK4 solver is now used in the temporal domain to simulate self-phase modulation, and to extract the broadened spectra. The spatially-averaged normalized spectrum  $S_{\text{avg}}^{(l)}(E)$  from a spatial intensity profile of an order  $l$  vortex is obtained by:

$$S_{\text{avg}}^{(l)}(E, \lambda) = \frac{1}{I_{\text{max}}^{(l)}} \iint \mathcal{S} \left( I^{(l)}(x, y, E), \lambda \right) \times I^{(l)}(x, y, E) dx dy \quad (5)$$

where  $E$  is the pulse energy,  $\mathcal{S} \left( I^{(l)}(x, y, E), \lambda \right)$  is the normalized broadened spectrum after  $14 \times 2$  mm of FS (the total amount seen by the pulse in the experimental setup) for a local intensity  $I^{(l)}(x, y, E)$ , and  $I_{\text{max}}^{(l)}$  is the maximum value of the

intensity.

The SPM is simulated at different intensities by assuming a plane wave propagator in the MPC, removing all possible spatio-temporal couplings in the laser beam. As the distribution in intensity is dependent on the order of the vortex, we again used Bayesian Optimization to compute the best scaling factor, shown in Fig. 3.

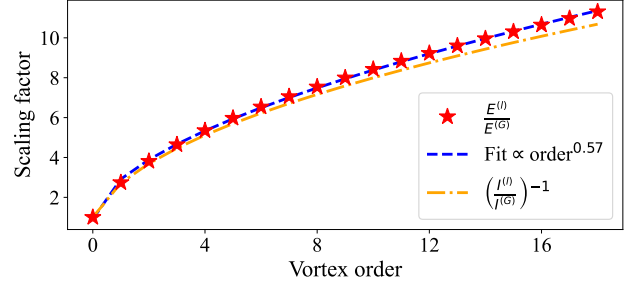


FIG. 3. Theoretical scaling derived using Bayesian Optimization to match the Gaussian FTL, from vortex order 0 to 18 (order 0 being a standard Gaussian).

The discrete data can be fitted using a power law  $l^{0.57}$  (in dashed blue in Fig. 3). Plotting the inverse of the intensity scaling law (Eq. 4), we see that the fit is close to this other scaling law (which can be approximated as  $\sqrt{2\pi}l$ ). We can intuitively understand this similarity in behavior: SPM is mainly influenced by the peak intensity of the temporal pulse, as it arises from the optical Kerr effect. As the intensity decreases with the vortex order, the effect of SPM will also decrease in the same way, and to compensate for the loss of non-linearity, the energy has to be increased to have the same peak intensity for all orders. From this power law scaling, one would want to use the highest order possible to increase the energy by a large factor. But as the vortex order increases, so does the size of the beam. Therefore, in practice, pushing towards the highest vortex orders might be limited by the size of the optical components.

## III. EXPERIMENTAL RESULTS

### A. Pulse post-compression setup

The experimental setup is shown in Fig. 4. The Ytterbium-based laser system is a PHAROS (*Light Conversion*) delivering 180 fs Full Width at Half Maximum (FWHM) pulses with energies up to 700  $\mu\text{J}$  and a repetition rate of 10 kHz. The initial beam profile is shown in the inset of Fig. 4. First, the beam is sent to a Spatial Light Modulator (*Hamamatsu Photonics*), used in reflection, to be shaped into a vortex beam. Such device uses liquid crystals to change the local refractive index experienced by the beam, thus imprinting a phase onto it. This way, one is able to generate any vortex beam and correct possible optical aberrations introduced by the setup.

At the exit of the laser, a manual attenuator consisting of a half-wave plate and a thin film polarizer is placed to study

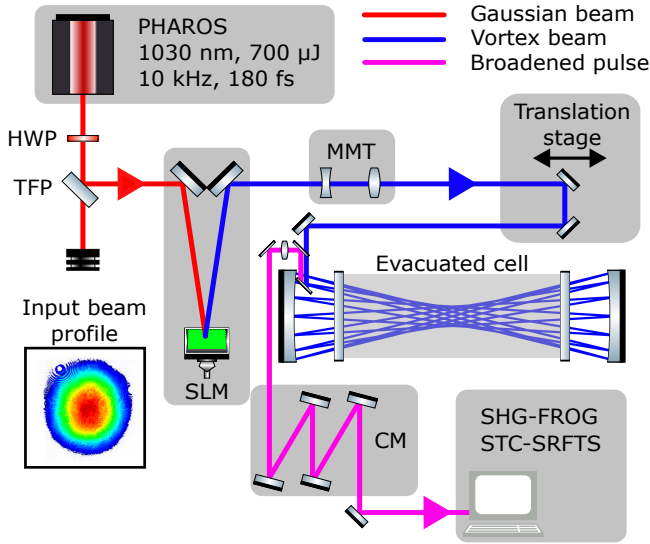


FIG. 4. Experimental setup for the use of vortex beams. SLM: Spatial Light Modulator, HWP: Half Wave Plate, TFP: Thin Film Polarizer, MMT: Mode-Matching Telescope, CM: Chirped Mirrors, SHG-FROG: Second Harmonic Generation - Frequency-Resolved Optical Gating, STC-SRFTS: Spatio-Temporal Couplings - Spatially-Resolved Fourier Transform Spectrometry. The initial beam profile is shown in the inset.

the energy scaling factor. After shaping by the SLM (with less than 2% losses), the beam is sent through an adjustable mode-matching lens telescope and a translation stage to allow tuning of the propagation distance to the MPC and adjusting the beam parameters following the results of Fig. 2. The beam is coupled into the MPC where it undergoes non-linear effects under 7 round-trips, each pass consisting of propagation through two 1 mm-thick anti-reflection coated FS plates, separated by 285 mm. The MPC mirrors have a 200 mm radius of curvature and are placed 382 mm apart. Between the plates, an evacuated cell (less than 10 mbar pressure) is placed to eliminate any non-linear effects from the air. The beam is coupled out of the cell, collimated and compressed using dispersive mirrors. The output compressed pulses are then characterized using in-house diagnostic devices, described in the following sections.

## B. Energy scaling results

The broadened spectrum of a pulse with a Gaussian spatial intensity profile is recorded after the MPC for three input pulse energies measured after the SLM (150  $\mu$ J, 175  $\mu$ J and 200  $\mu$ J). Then, for different vortex orders, the spectral widths are matched to these Gaussian-equivalent references, by tuning the input pulse energy.

In Fig. 5, the spatially-averaged spectra taken for a Gaussian-equivalent broadening at 200  $\mu$ J, and measured using an integrating sphere, are presented. The corresponding input energies are indicated in Table I.

The scaling shows a significant increase of the input pulse

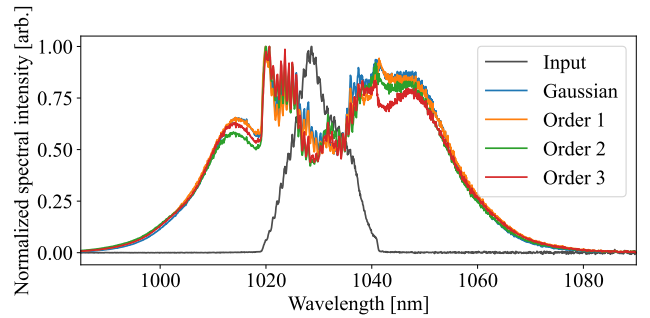


FIG. 5. Experimental spectra for a Gaussian-equivalent broadening of 200  $\mu$ J for  $l = 1 - 3$ . The initial spectrum from the laser is shown in black.

TABLE I. Corresponding input pulse energies and the average energy scaling factor.

	Gaussian	Order 1	Order 2	Order 3
	150 $\mu$ J	270 $\mu$ J	343 $\mu$ J	450 $\mu$ J
	175 $\mu$ J	315 $\mu$ J	396 $\mu$ J	530 $\mu$ J
	200 $\mu$ J	350 $\mu$ J	451 $\mu$ J	610 $\mu$ J
Average energy scaling factor		1.8	2.3	3.0

energy that can be sent into the MPC for the same broadening compared to a Gaussian beam, up to a factor 3 using a vortex of order 3. It has to be noted that this scaling is slightly lower than the predicted factor in II C,  $\approx 4.5$ . This is due to the fact that the simulations are performed with an ideal homogeneous vortex beam, free from any localized intensity variations that could induce a stronger spectral broadening. In our experimental setup, because of the SLM segmentation, the beams can carry hotspots, which reduce the energy needed to have the same peak intensity as compared to an ideal vortex (see III C). Consequently, this also affects the non-linear propagation. The downside of using large orders is that the beam size is already doubled with an order 3 vortex. However, the vortex of order 3 still fits on the in- and out-coupling mirror, which is the smallest optical component of the MPC. The transmission of the cell remains above 90% for all measurements, ensuring that there is no losses due to ionization or clipping.

The MPC output is compressed using 12 bounces on dispersive mirrors, compensating a total GDD of 2400 fs<sup>2</sup>. The resulting pulses are characterized using second harmonic generation frequency-resolved optical gating (SHG-FROG)<sup>28</sup> with no spatial sampling. In Fig. 6, the retrieved temporal profiles corresponding to a 200  $\mu$ J Gaussian-equivalent spectral broadening are shown. The compression is optimized for the 200  $\mu$ J Gaussian spatial intensity profile.

From the retrievals we see that all pulses are similar to the Gaussian case, implying that there is no effect on the temporal properties other than the scaling in energy and peak power as observed in Fig. 6. We retrieve pulses between 42 fs and 47 fs FWHM, with an FTL around 42 fs. We also see a clear effect from Third Order Dispersion (TOD), which leads to a side pulse. The TOD is most likely coming from the many

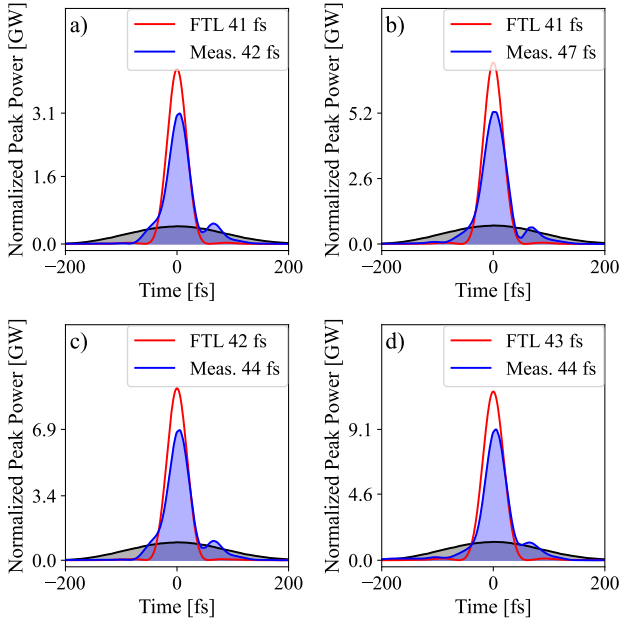


FIG. 6. SHG-FROG retrievals (blue) and FTL profiles (red) at 200  $\mu$ J Gaussian-equivalent broadening for a) Gaussian, b) order 1 vortex, c) order 2 vortex and d) order 3 vortex. The SHG-FROG retrieval of the input laser pulse is shown in black.

reflections on dispersive mirrors, which only allow control of the GDD. Yet, the main pulse contains  $> 80\%$  of the pulse energy, enabling further experimental utilization.

Using the data from Table I, the transmission of the post-compression setup and the FROG retrievals, the peak powers can be estimated. In Table II, the peak powers recorded at 200  $\mu$ J Gaussian-equivalent broadening are summarized. A maximum output peak power of 9.1 GW was reached for a vortex of order 3, corresponding to a factor 3.6 increase. Providing that the spectral phase could be fully compensated for, one could achieve a peak power of 11.7 GW.

TABLE II. Peak power scaling for equivalent broadenings.

	Gaussian	Order 1	Order 2	Order 3
Input peak power (GW)	0.8	1.5	1.9	2.5
Output peak power (GW)	3.1	5.3	6.9	9.1
Peak power boost	3.9	3.5	3.6	3.6

### C. Spatial characterization of vortices

The spatial characterization of vortex beams is not straightforward, as there is no consensus on how to assess the homogeneity of a ring beam. As the propagation still follows the Gaussian formalism, one could perform an  $M^2$  measurement<sup>29</sup>, normalized to the theoretical vortex beam size (see Eq. 3). Yet, this quantity can be blind to the spatial quality of the considered vortices. We propose hereafter

the definition of two parameters, the angular Intensity Homogeneity (IH) and the angular Width Homogeneity (WH), to classify the global Ring Homogeneity (RH) of the generated and propagated beams.

First, IH quantifies the variations of intensity maxima on different diameter-cuts through the center of the vortex beam. By taking  $n$  cuts over different angles into account, we can define IH as:

$$\text{IH} = \frac{1}{n} \sum_{k=1}^n \left| \frac{I(P_{1,k}) - I(P_{2,k})}{I(P_{1,k}) + I(P_{2,k})} \right|, \quad 0 \leq \text{IH} \leq 1 \quad (6)$$

with  $I(P_{1,k})$  and  $I(P_{2,k})$  the intensities of the two main peaks over the  $k$ -th considered diameter of the ring. This operator is blind to the spread of each peak, that can come from aberrations. Thus, we define WH as:

$$\text{WH} = \frac{1}{n} \sum_{k=1}^n \left| \frac{\sigma(P_{1,k}) - \sigma(P_{2,k})}{\sigma(P_{1,k}) + \sigma(P_{2,k})} \right|, \quad 0 \leq \text{WH} \leq 1 \quad (7)$$

where  $\sigma(P_{1,k})$  and  $\sigma(P_{2,k})$  are the FWHM of the peaks over the  $k$ -th considered diameter. In Fig. 7 a), an example of the characterization is shown, highlighting the considered parameters.

Using these two parameters, the homogeneity of  $\text{LG}_{0,l}$  beams is quantified as  $\text{RH} = (\text{IH}; \text{WH})$ , with the ideal beam tending towards (0;0). In Fig. 7 b), the spatial profiles of the beams are shown before and after a 200  $\mu$ J Gaussian-equivalent broadening in the MPC, for the three first vortex orders. The value of RH are indicated in Table III for each beam profile, and a graphical representation is shown in Fig. 7 c).

TABLE III. Ring Homogeneity parameters for input and output beams.

Order	Position	IH	WH
1	In	$2.0 \times 10^{-1}$	$7.1 \times 10^{-2}$
	Out	$1.6 \times 10^{-1}$	$1.3 \times 10^{-1}$
2	In	$1.4 \times 10^{-1}$	$1.2 \times 10^{-2}$
	Out	$1.0 \times 10^{-1}$	$2.5 \times 10^{-2}$
3	In	$1.4 \times 10^{-1}$	$2.0 \times 10^{-2}$
	Out	$1.2 \times 10^{-1}$	$3.7 \times 10^{-2}$

After shaping by the SLM, the vortices, shown in Fig. 7 b) I, II and III, exhibit a large diffraction pattern (in blue) due to the phase singularity on the SLM. This pattern disappears after propagation through the MPC, as displayed in Fig. 7 b) IV, V and VI. The IH decreases while the WH slightly increases after spectral broadening. Yet, the vortices are still consistent with their non-broadened spatial profiles, which ensures that the propagation through the MPC is maintaining satisfactory spatial properties for further applications.

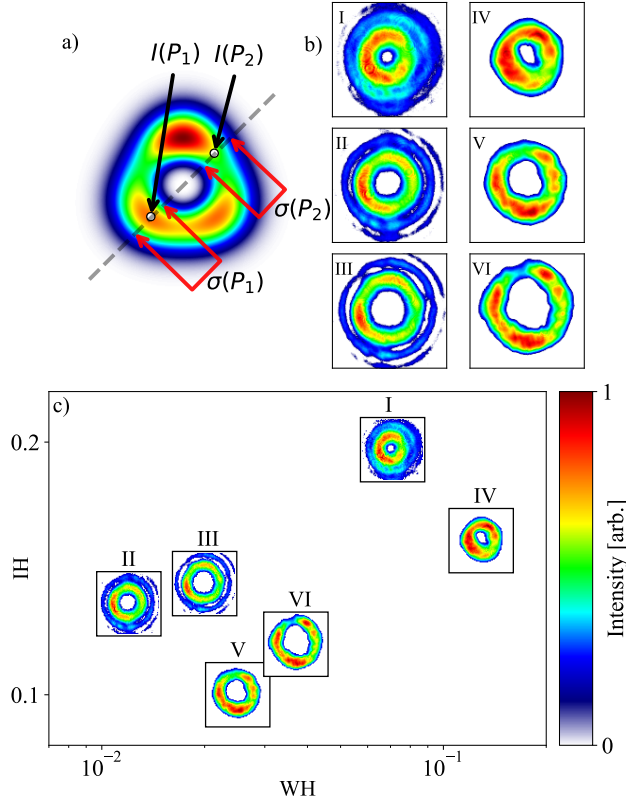


FIG. 7. a) Example of a RH characterization on a simulated inhomogeneous vortex, with the relevant parameters only shown over one cut. b) Spatial profiles of the collimated beams before (I:  $l = 1$ , II:  $l = 2$ , III:  $l = 3$ ) and after the MPC (IV:  $l = 1$ , V:  $l = 2$ , VI:  $l = 3$ ). c) Graphical representation of the RH for the considered profiles. The colorbar representing the normalized intensity is common to all the spatial profiles.

#### D. Spatio-temporal characterization of vortices

A spatio-temporal characterization of the pulses is performed using spatially-resolved Fourier transform spectrometry<sup>30</sup>. The setup normally uses a reference beam that is generated by focusing the same laser into a tight spot. Its central part is then sampled as reference for the measurement, which is not possible with a vortex that carries a hole. Instead, we use a particular property of SLMs, which is that they only work for a specific polarization state (in our case S-polarization). The input polarization can be rotated so that the S-polarized component experiences the phase imprint from the SLM to form a vortex beam, while the P-polarized component does not experience a phase imprint and therefore remains Gaussian. By tuning the input polarization angle, the energy ratio between the two beams is changed so that both pulses with different spatial profiles undergo the same amount of spectral broadening in the MPC. The experimental setup is shown in Fig. 8. After the post-compression setup, the pulse with a vortex beam and the reference pulse with a Gaussian beam are split by a polarization beam splitter. The

Gaussian profile gets its polarization rotated to match that of the vortex beam, is then sent to a delay stage and focused with an off-axis parabola to generate a spherical wavefront (a small portion of which is later selected via a pinhole). The two pulses are then recombined by a second beam splitter, and their interference pattern is recorded on a camera for different delays.

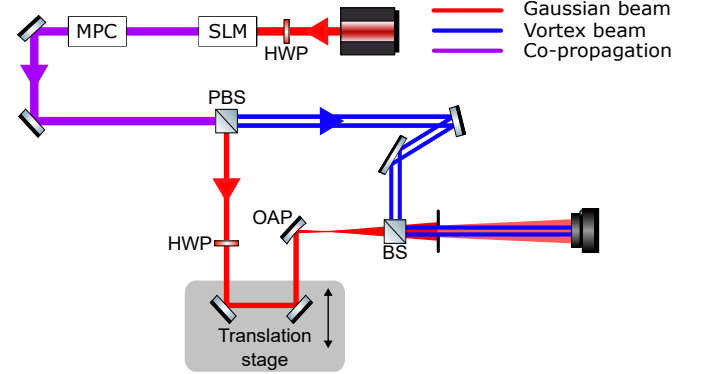


FIG. 8. Experimental spatio-temporal measurement setup. PBS: Polarization Beam Splitter, BS: Beam Splitter, HWP: Half-Wave Plate, OAP: Off-Axis Parabola.

As a proof of concept, we measure the spatio-temporal profile of a vortex of order 1, at a Gaussian-equivalent broadening of  $150\mu\text{J}$ , i.e.  $150\mu\text{J}$  for the Gaussian beam and  $270\mu\text{J}$  for the vortex beam, for a total of  $420\mu\text{J}$  input pulse energy. A higher pulse energy could be used to maximize the spectral broadening, but was not considered at this time, as the goal was to simply test the method with relaxed pulse parameters. For further experimental studies utilizing the post-compressed pulses, spatio-temporal characterization will be performed at full energy.

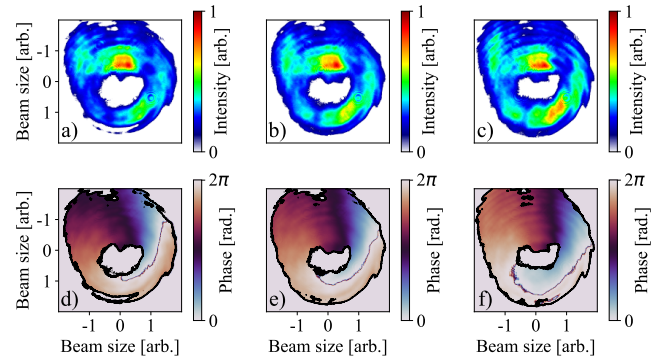


FIG. 9. Intensity and phase distributions for  $\lambda = 1010\text{ nm}$  [a) and d)],  $1030\text{ nm}$  [b) and e)],  $1050\text{ nm}$  [c) and f)].

The underlying assumption for this measurement to be valid is that the only non-linear effect acting on the pulses is the SPM. However, due to the co-propagation of two waves with similar intensities, a discussion is needed regarding potential cross-phase modulation (XPM). First, the two pulses do not share the same polarization and they are not temporally overlapped, as the SLM is pseudo-birefringent (only one

polarization sees the phase pattern). Secondly, the maxima of the beams are not spatially overlapping, as a vortex beam is by definition hollow. The comparison of the broadened spectra after the MPC for a vortex-only beam and co-propagating vortex and Gaussian beams leads to very little disparities, which indicates that spectral broadening is still dominated by the SPM. For higher energies, the addition of a proper birefringent crystal would ensure a temporal separation large enough to avoid any XPM.

From the STC measurement, the intensity and phase distributions at three different wavelengths are extracted and displayed in Fig. 9 a)-f), for  $\lambda = 1010$  nm (a) and d)), 1030 nm (b) and e)) and 1050 nm (c) and f)). The three intensity profiles are close to identical, and the three phases exhibit a spiral pattern that is highly similar for all wavelengths. The average ring homogeneity is (0.11;0.78), which is far from the values at the output of the MPC in Table III. The WH is especially high, due to a measurement artifact that is seen at the top of the profiles. In our case, shaping the beam of a narrow-band pulse with an SLM before spectral broadening allows mitigating losses arising from spectrally-dependent phase imprint. Thus, short pulses can be generated with an "achromatic OAM" for all wavelengths.

#### IV. CONCLUSIONS

Using a Laguerre-Gaussian single-vortex intensity profile inside a 382 mm long bulk multi-pass cell enables the pulse energy scaling of such post-compression method with a factor 1.8 for vortex of order 1 and up to a factor 3 for an order 3, compared to propagation with a Gaussian spatial profile. Pulses with 180 fs duration and 610  $\mu$ J pulse energy, corresponding to 2.5 GW input peak power, are compressed down to 44 fs, with a spatial homogeneity suitable for further experimental use. Despite the somewhat large peak powers employed in the bulk MPC, the spatial distribution is unchanged across the broadened spectrum. Moreover, the topological charge is shown to be conserved after non-linear propagation and kept constant across the spectrum. The utilization of an SLM, aside from shaping the beam and making the transition between vortices of different orders extremely simple, allows the precise control of the input intensity and phase profile, something that is not possible with simple spiral phase plates. Aberrations are also corrected to optimize the output beam quality and maximize the throughput of the MPC. The output peak power reached in such compact setup is 9.1 GW, which is, to the best of our knowledge, a state-of-the-art result for a single-stage Herriott-type bulk MPCs, similar to recent results<sup>31</sup>, with however  $> 500 \mu$ J pulse energies. While this is still far from the record peak powers attained in gas-filled MPCs<sup>9</sup> and HCF<sup>16</sup>, the compactness and low complexity of the setup is attractive for laser systems with more relaxed parameters. In our experiment, the maximum pulse energy available from the source (700  $\mu$ J) could almost be entirely used, and we foresee that the scaling technique presented here should easily enable compression of mJ-level pulses with higher-order vortices. Though, the increased

beam size of vortices implies the use of larger optics, or possibly segmented optical components, which goes against the idea of a simple, compact experimental setup. In this case, spatial beam shaping can be combined with other innovative cell geometries to reduce the overall footprint<sup>20,21</sup>. Efficiently removing the vortex geometry with the increased bandwidth is also a challenge for experiments requiring a Gaussian-like profile. Phase plates and SLMs can undo the OAM, but the reconstruction of a Gaussian profile would call for additional design. Nevertheless, the direct use of vortices is highly interesting for, e.g., HHG<sup>32</sup> and LPA<sup>33</sup>. In particular, high resolution ptychography benefits from OAM beams carrying more phase information in retrievals<sup>34,35</sup>.

#### FUNDINGS

The authors acknowledge financial support from the Swedish Research Council (Grants Nos. 2021-04691 and 2022-03519) and the Crafoord Foundation.

#### ACKNOWLEDGMENTS

The authors would like to thank Peter Smorenburg and David O'Dwyer from ASML for fruitful discussions and helpful suggestions during the writing of the paper.

#### DISCLOSURES

The authors declare no conflicts of interest.

#### AUTHOR CONTRIBUTIONS

**V. K.:** Conceptualization (main); Data curation (main); Formal analysis (main); Investigation (main); Methodology (equal); Software (main); Validation (equal); Visualization (main); Writing – original draft (main). **S. W.:** Data curation (equal); Formal analysis (equal); Investigation (equal); Methodology (equal); Validation (equal); Writing – review and editing (supporting). **M. R.:** Methodology (equal); Investigation (supporting); Software (supporting); Writing – review and editing (supporting). **G. B.:** Investigation (supporting); Writing – review and editing (supporting). **A.-K. R.:** Methodology (supporting); Writing – review and editing (supporting). **C. G.:** Methodology (supporting); Writing – review and editing (supporting). **C. L. A.:** Methodology (supporting); Writing – review and editing (supporting). **A.-L. V.:** Conceptualization (main); Funding acquisition (main); Investigation (equal); Methodology (equal); Project administration (main); Supervision (main); Writing – review and editing (equal).

## DATA AVAILABILITY STATEMENT

The data that support the findings of this study are available from the corresponding author upon reasonable request.

## REFERENCES

- <sup>1</sup>R. Klas, W. Eschen, A. Kirsche, J. Rothhardt, and J. Limpert, “Generation of coherent broadband high photon flux continua in the XUV with a sub-two-cycle fiber laser,” *Opt. Express* **28**, 6188–6196 (2020).
- <sup>2</sup>B. Farace, J. Osterhoff, E. Escoto, K. Poder, W. Leemans, N. Khodakovskiy, C. Heyl, R. Shaloo, and S. Rajhans, “A plasma accelerator driven by an industrial Yb:YAG laser at kHz repetition rate,” in *European Advanced Accelerator Concepts Workshop*, PUBDB-2023-08093 (PAs for Industrial and Health Applications, 2023).
- <sup>3</sup>T. Nagy, P. Simon, and L. Veisz, “High-energy few-cycle pulses: post-compression techniques,” *Advances in Physics: X* **6**, 1845795 (2021).
- <sup>4</sup>J. Schulte, T. Sartorius, J. Weitenberg, A. Vernaleken, and P. Russbueldt, “Nonlinear pulse compression in a multi-pass cell,” *Opt. Lett.* **41**, 4511–4514 (2016).
- <sup>5</sup>A.-L. Viotti, M. Seidel, E. Escoto, S. Rajhans, W. P. Leemans, I. Hartl, and C. M. Heyl, “Multi-pass cells for post-compression of ultrashort laser pulses,” *Optica* **9**, 197–216 (2022).
- <sup>6</sup>D. Herriott, H. Kogelnik, and R. Kompfner, “Off-axis paths in spherical mirror interferometers,” *Appl. Opt.* **3**, 523–526 (1964).
- <sup>7</sup>M. Kaumanns, V. Pervak, D. Kormin, V. Leshchenko, A. Kessel, M. Ueffing, Y. Chen, and T. Nubbemeyer, “Multipass spectral broadening of 18 mJ pulses compressible from 1.3 ps to 41 fs,” *Opt. Lett.* **43**, 5877–5880 (2018).
- <sup>8</sup>Y. Pfaff, G. Barbiero, M. Rampp, S. Klingebiel, J. Brons, C. Y. Teisset, H. Wang, R. Jung, J. Jaksic, A. H. Woldegeorgis, *et al.*, “Nonlinear pulse compression of a 200 mJ and 1 kW ultrafast thin-disk amplifier,” *Opt. Express* **31**, 22740–22756 (2023).
- <sup>9</sup>S. Rajhans, E. Escoto, N. Khodakovskiy, P. K. Velpula, B. Farace, U. Grosse-Wortmann, R. J. Shaloo, C. L. Arnold, K. P. oder, J. Osterhoff, W. P. Leemans, I. Hartl, and C. M. Heyl, “Post-compression of multi-millijoule picosecond pulses to few-cycles approaching the terawatt regime,” *Opt. Lett.* **48**, 4753–4756 (2023).
- <sup>10</sup>S. Hädrich, E. Shestaeu, M. Tschernajew, F. Stutzki, N. Walther, F. Just, M. Kienel, I. Seres, P. Jójárt, Z. Bengery, *et al.*, “Carrier-envelope phase stable few-cycle laser system delivering more than 100 W, 1 mJ, sub-2-cycle pulses,” *Opt. Lett.* **47**, 1537–1540 (2022).
- <sup>11</sup>S. Gröbmeyer, K. Fritsch, B. Schneider, M. Poetzlberger, V. Pervak, J. Brons, and O. Pronin, “Self-compression at 1  $\mu\text{m}$  wavelength in all-bulk multi-pass geometry,” *Appl. Phys. B* **126**, 1–6 (2020).
- <sup>12</sup>J. Marburger, “Self-focusing: Theory,” *Progress in Quantum Electronics* **4**, 35–110 (1975).
- <sup>13</sup>A.-K. Raab, M. Seidel, C. Guo, I. Sytcevech, G. Arisholm, A. L’Huillier, C. L. Arnold, and A.-L. Viotti, “Multi-gigawatt peak power post-compression in a bulk multi-pass cell at a high repetition rate,” *Opt. Lett.* **47**, 5084–5087 (2022).
- <sup>14</sup>M. Hanna, L. Daniault, F. Guichard, N. Daher, X. Delen, R. Lopez-Martens, and P. Georges, “Nonlinear beam matching to gas-filled multipass cells,” *OSA Continuum* **4**, 732–738 (2021).
- <sup>15</sup>M. Seidel, P. Balla, C. Li, G. Arisholm, L. Winkelmann, I. Hartl, and C. M. Heyl, “Factor 30 pulse compression by hybrid multipass multiplate spectral broadening,” *Ultrafast Science* **2022** (2022).
- <sup>16</sup>G. Fan, P. Carpeggiani, Z. Tao, G. Coccia, R. Safaei, E. Kaksis, A. Pugzlys, F. LÉgaré, B. Schmidt, and A. Baltuška, “70 mJ nonlinear compression and scaling route for an Yb amplifier using large-core hollow fibers,” *Opt. Lett.* **46**, 896–899 (2021).
- <sup>17</sup>A. Omar, M. Hoffmann, G. Galle, F. Sylla, and C. J. Saraceno, “Hybrid air-bulk multi-pass cell compressor for high pulse energies with full spatio-temporal characterization,” *Opt. Express* **32**, 13235–13248 (2024).
- <sup>18</sup>V. Hariton, K. Fritsch, K. Schwarz, N. Kovalenko, G. Figueira, G. Arisholm, and O. Pronin, “Spectral broadening in convex-concave multipass cells,” *Opt. Express* **31**, 19554–19568 (2023).
- <sup>19</sup>A. Omar, T. Vogel, M. Hoffmann, and C. J. Saraceno, “Spectral broadening of 2-mJ femtosecond pulses in a compact air-filled convex-concave multipass cell,” *Opt. Lett.* **48**, 1458–1461 (2023).
- <sup>20</sup>C. M. Heyl, M. Seidel, E. Escoto, A. Schönberg, S. Carlström, G. Arisholm, T. Lang, and I. Hartl, “High-energy bow tie multi-pass cells for nonlinear spectral broadening applications,” *J. Phys. Photonics* **4**, 014002 (2022).
- <sup>21</sup>A. Schönberg, S. Rajhans, E. Escoto, N. Khodakovskiy, V. Hariton, B. Farace, K. Pöder, A.-K. Raab, S. Westerberg, M. Merdanov, *et al.*, “Compact, folded multi-pass cells for energy scaling of post-compression,” arXiv preprint arXiv:2409.02542 (2024).
- <sup>22</sup>H. Stark, C. Grebing, J. Buldt, A. Klenke, and J. Limpert, “Divided-pulse nonlinear compression in a multipass cell,” *J. Phys. Photonics* **4**, 035001 (2022).
- <sup>23</sup>M. Kaumanns, D. Kormin, T. Nubbemeyer, V. Pervak, and S. Karsch, “Spectral broadening of 112mJ, 1.3ps pulses at 5kHz in a LG10 multipass cell with compressibility to 37fs,” *Opt. Lett.* **46** 5, 929–932 (2021).
- <sup>24</sup>L. T. Vuong, T. D. Grow, A. Ishaaya, A. L. Gaeta, G. W. ’t Hooft, E. R. Eiel, and G. Fibich, “Collapse of optical vortices,” *Phys. Rev. Lett.* **96**, 133901 (2006).
- <sup>25</sup>R. L. Phillips and L. C. Andrews, “Spot size and divergence for laguerre gaussian beams of any order,” *Appl. Opt.* **22**, 643–644 (1983).
- <sup>26</sup>C. Runge, “On the numerical solution of differential equations,” *Mathematical Annals* **46**, 167–178 (1895).
- <sup>27</sup>F. Nogueira, “Bayesian Optimization: Open source constrained global optimization tool for Python,” (2014).
- <sup>28</sup>D. J. Kane and R. Trebino, “Characterization of arbitrary femtosecond pulses using frequency-resolved optical gating,” *IEEE J. of Quantum Electr.* **29**, 571–579 (1993).
- <sup>29</sup>H. Fathi, M. Närhi, R. Barros, and R. Gumenyuk, “Coherent beam combining of optical vortices,” *Opt. Lett.* **49**, 3882–3885 (2024).
- <sup>30</sup>M. Miranda, M. Kotur, P. Rudawski, C. Guo, A. Harth, A. L’Huillier, and C. L. Arnold, “Spatiotemporal characterization of ultrashort laser pulses using spatially resolved fourier transform spectrometry,” *Opt. Lett.* **39**, 5142–5145 (2014).
- <sup>31</sup>Y. Liu, Z. Chen, S. Yang, Y. He, X. Wang, Y. Ma, C. Zhou, and S. Fang, “Few-cycle 12.5-Gw pulses generated via efficient all-solid-state post-compression from an ytterbium laser,” *Opt. Lett.* **49** 24, 6992–6995 (2024).
- <sup>32</sup>C. Hernández-García, L. Rego, J. San Román, A. Picón, and L. Plaja, “Attosecond twisted beams from high-order harmonic generation driven by optical vortices,” *High Power Laser Science and Engineering* **5** (2017), 10.1017/hpl.2017.1.
- <sup>33</sup>H. Song, K. H. Pae, J. Won, J. Song, S. Lee, C. M. Kim, C.-M. Ryu, W. Bang, and C. H. Nam, “Characteristics of electron beams accelerated by parallel and antiparallel circularly polarized Laguerre-Gaussian laser pulses,” *Appl. Phys. B* **129**, 56 (2023).
- <sup>34</sup>B. Wang, N. J. Brooks, P. Johnsen, N. W. Jenkins, Y. Esashi, I. Binnie, M. Tanksalvala, H. C. Kapteyn, and M. M. Murnane, “High-fidelity ptychographic imaging of highly periodic structures enabled by vortex high harmonic beams,” *Optica* **10**, 1245–1252 (2023).
- <sup>35</sup>C. Hernández-García, J. Vieira, J. T. Mendonça, L. Rego, J. San Román, L. Plaja, P. R. Ribic, D. Gauthier, and A. Picón, “Generation and applications of extreme-ultraviolet vortices,” *Photonics* **4** (2017).